Effect of particle non-sphericity on satellite monitoring of drifting volcanic ash clouds — Source link [↗]

Nickolay A. Krotkov, D. E. Flittner, Arlin J. Krueger, Alexander B. Kostinski ...+3 more authors

Institutions: Raytheon, University of Arizona, Goddard Space Flight Center, Michigan Technological University ...+1 more institutions

Related papers:

- Modeling phase functions for dustlike tropospheric aerosols using a shape mixture of randomly oriented polydisperse spheroids

- Retrieval of sizes and total masses of particles in volcanic clouds using AVHRR bands 4 and 5

- Quantitative shape measurements of distal volcanic ash

- Light scattering in planetary atmospheres

- Scattering matrices of mineral aerosol particles at 441.6 nm and 632.8 nm

EFFECT OF PARTICLE NON-SPHERICITY ON SATELLITE

MONITORING OF DRIFTING VOLCANIC ASH CLOUDS

N.A. Krotkov[1]

Raytheon ITSS Corp., Lanham, MD 20706

D.E. Flittner

University of Arizona, Tucson, AZ 85721

A.J. Krueger, A. Kostinski [2]

Laboratory for Atmospheres, NASA/GSFC, Greenbelt, MD 20770

C. Riley and W. Rose

Michigan Technological University, Houghton, MI 49931

December 15, 1998

Table of contents

---

[1] Corresponding author address: Nicholay A. Krotkov, Raytheon STX Corporation, 4400 Forbes Boulevard, Lanham, MD 20706; krotkov@hoss.stx.com

2 On subbatical leave from Phys. Dept., Michigan Tech. University, USRA/Goddard visiting scientist program

1. INTRODUCTION

Volcanic eruptions loft gases and ash particles into the atmosphere and produce effects that are both short term (aircraft hazards, interference with satellite measurements) and long term (atmospheric chemistry, climate). Large (>0.5mm) ash particles fall out in minutes [Rose et al, 1995], but fine ash particles can remain in the atmosphere for many days. This fine volcanic ash is a hazard to modern jet aircraft because the operating temperatures of jet engines are above the solidus temperature of volcanic ash, and because ash causes abrasion of windows and airframe, and disruption of avionics. At large distances($10^2 - 10^4$km or more) from their source, drifting ash clouds are increasingly difficult to distinguish from meteorological clouds, both visually and on radar [Rose et al., 1995]. Satellites above the atmosphere are unique platforms for viewing volcanic clouds on a global basis and measuring their constituents and total mass. Until recently, only polar AVHRR and geostationary GOES instruments could be used to determine characteristics of drifting volcanic ash clouds using the 10-12μm window [Prata 1989; Wen and Rose 1994; Rose and Schneider 1996]. The NASA Total Ozone Mapping Spectrometer (TOMS) instruments aboard the Nimbus-7, Meteor3, ADEOS, and Earth Probe satellites have produced a unique data set of global S02 volcanic emissions since 1978 (Krueger et al., 1995). Besides S02, a new technique has been developed which uses the measured spectral contrast of the backscattered radiances in the 330-380nm spectral region (where gaseous absorption is negligible) in conjunction with radiative transfer models to retrieve properties of volcanic ash (Krotkov et al., 1997) and other types of absorbing aerosols (Torres et al., 1998).

Until now both UV and IR ash retrieval models assume sphericity of the ash particles [Wen and Rose 1994; Krotkov et al.1997; Torres et al, 1998]. In this paper a first attempt is made to study the effect of nonsphericity on the accuracy of the of ash optical thickness and effective radius retrievals from the TOMS UV reflectance measurements. First, we analyze the available measurements of the ash fallout samples from the August 19, 1992 Mt. Spurr (Alaska) eruption to characterize particle shape distributions, as well as the index of refraction at TOMS wavelengths. Next, we simulate scattering properties of the Mt.Spurr ash cloud using a model of randomly oriented spheroids and the T-matrix method (Mishchenko and Travis 1998, here-after MT). Finally, we estimate the retrieval errors of the TOMS UV reflectance technique caused by ash non-sphericity.

2. MEASUREMENTS OF MT. SPURR ASH FALLOUT SAMPLES

Volcanic ash particles have a wide distribution of shapes and sizes. Since the airborne ash particles are difficult to collect, fallout samples are often the only samples available for direct measurements. Samples of ash fallout from the August 19, 1992 Mt. Spurr eruption were collected and analyzed for grain size and shape distribution. Samples were collected at Wells Bay (~225 km east of Mt. Spurr in an area of secondary thickening of the ash deposit) and Yakutat (~650 km east of Mt. Spurr at the most distant region of fallout).

Volcanic ash is composed of about 60-100% silicate glass with 50-78wt% SiO_2. The remaining fraction of the ash is silicate mineral grains. The dominant glass material is an exploded froth with bubbles that typically range from 1 micron to 1 mm or more in diameter. Many of the ash particles shown in the figures are fragments of bubble walls (shards). Rose [1986] gives details of the character of ash.

2.1 *Size Distributions*

The size distributions of the samples from each site were measured using low angle forward Fraunhoffer analysis. This method works by floating particles in water past a laser beam. The amount of scatter by the laser beam is related to an equivalent spherical particle radius, r. For the Yakutat sample, the mean particle radius was 20.6 μm (10% of the particles have r< 3.0 μm, 50% have r < 18.7 μm, 80% have r< 33.6μm). The particles were larger for the Wells Bay sample (mean radius 39.3 μm, 10% r< 3.8 μm, 50% r < 23.1μm, 80% r < 73.0μm).

2.2 *Shape Characterization*

Shape characteristics were determined for the same samples using the following procedure. The Wells Bay sample was seperated into 18 subsamples using air elutriation. Each subsample contains particles that were suspended by a specific air flow rate and so represent groups of particles having specific terminal settling velocity ranges. The air flow rates chosen for each terminal velocity group correspond to flow rates used to suspend spherical particles with specific diameters (listed in Table 1). Subsamples of the Yakutat sample were not made. Ash from the Wells Bay subsamples and Yakutat sample were deposited on aluminum stubs by first unclumping the charged particles with a destat gun. Ash was then sprinkled through a hole in the side of a funnel into a fast moving air stream where the ash particles are transported to a grain mount held ~8cm from the end of the funnel. Particles stick to the surface of the aluminum stub by adhering to a carbon sticky tab on the surface. Both the distance between the aluminum stub and funnel and the air flow rate were selected to provide the best particle separation and random particle orientation.

The SEM backscattered images were taken of 43 to 145 particles in each size bin. The magnification was set so that the greatest number of particles were observed at an adequate separation. This enables the automated image analysis system to correctly distinguish individual particles. Figure 1 shows a SEM image of the particles in the smallest bin from the Wells Bay sample (terminal velocity group one, Table 1). Particles are typically light in color as compared to the black carbon background, providing a nearly binary image. These images were imported into an image analysis program, where a bit map was made to highlight the ash particles. Aspect ratios for terminal velocity group 1 may contain some error since these particles are very small (<10 μm) and particle resolution is poor which causes particles to appear slightly blurred. A trap function is used to eliminate ash particles less than 5 by 5 pixels, since such particles are too small to be accurately measured by the computer. Particles that are cut off at the edge of an image are also eliminated and the remaining particles are measured for aspect ratio and other spahe parameters (length, width, fractal dimension, sphericity, and shape factor). Since we use the model of spheroids, only the mean aspect ratio was used in the calculations. To determine the longest length and the shortest width for the aspect ratio estimation, 64 ferrets were measured for each particle image. A ferret is defined as the distance between two tangents taken on opposite sides of the particle projection. **Table 1** lists the minimum, maximum, and mean aspect ratios (length/width) for ash from Mt. Spurr. **Figure 2** shows the aspect ratio distribution in the finest size group (group 1 in Table 1).

We note some problems with this method of measuring particle shapes. First, we assume that the air stream provides randomly oriented particles on the aluminum stubs -this appears true since we see particles lying flat and on edge, but is difficult to prove. We also note that single angle projection measurements (2D) tend to underestimate the true mean (3D) aspect ratio just by

the mere fact of taking a projection. As Okada et al [1987] pointed out, "... it is impossible to access the three-dimensional shape of particles unambiguously...". Indeed, the exact reconstruction of 3D aspect ratios from 2D projection measurements is still an unresolved problem [Santalo, chapter 16, pp. 291-292, 1976]. We note, however, that for convex particles the error should decrease with decreasing in the particle mean aspect ratio, which is close to 1.5 for overall 1,297 particles of the Wells Bay sample (Table 1). For this range of 2D aspect ratios our estimates with simple particle shapes (rectangular, cylinder) indicate possible underestimation of the 3D aspect ratio of the order of 10% -20%. Non-convex particles are not considered in this paper.

Since the ash samples were collected from the ground, a problem arises as to how these measurements are representative of the finest airborne ash fraction? To address this problem, we compared the mean aspect ratios separately for different particle size ranges. The results of these comparisons show very little change in aspect ratio between different size ranges (Table 1). The particles in the finest size range have aspect ratios close to 1.5. Aspect ratios from the Wells Bay sample are close to those of the more distant Yakutat sample. This analysis suggests that the mean measured aspect ratio of the fallout sample can be used to represent the finest fraction of the Spurr ash, expected to be observed by remote sensing instruments.

One important feature of ash falls is that larger particles tend to collect or aggregate smaller ones. Thus the smaller size fractions in the fallout ashes we studied were too fine to have fallen out as simple particles. Thus, we think that size determinations of these particles closely resemble those of similar size particles that remained in the drifting cloud.

2.3 Refractive index measurements

Measurements of the complex refractive index of the same ash fallout samples at the TOMS

wavelengths (300nm- 400nm) were conducted using different techniques (Winchester, 1998).

The real component, n_r, was determined by measuring the sample reflectance at a $0°$ angle of

incidence whereas the imaginary component, n_i, was determined by measuring the Kubelka-

Munk coefficients of a diluted sample. The sample was prepared by mixing known amounts of

the ash and barium sulphate ($BaSO4$). The mixture was pressed into a pellet and placed in a

sample holder inside a 4-inch integrating sphere to measure the diffuse reflectance of the sample.

A Xe lamp (PowerArc from Photon Technology International) provided direct illumination of the

sample. The reflected diffuse radiation was detected with a photomultiplier tube (R928 from

Hamamatsu), using a spectrometer (SP-150 from Acton Research Corporation, 2nm resolution)

as a filter. The measured diffuse reflectance of the mixture was then used in the Kubelka-Munk

function to estimate the bulk absorption coefficient of the ash. This technique has been

previously used to measure absorption properties of volcanic ash [Patterson 1981] and dust

aerosols [Patterson et al., 1977]. The real component of the refractive index was determined by

evaluating the Fresnel equation for nadir reflection of the pressed pure ash sample. The

reflectance measurements for computing n_i and n_r were reproducible to within 1%.

The imaginary part of the refractive index is relatively flat with wavelength for all ash

samples. For simplicity, in the following sections we neglect the very slight spectral variation of

refractive index between TOMS wavelengths of 340nm, 360nm, and 380nm, (1.53 - i0.0050,

1.52 - i0.0048, and 1.55 - i0.0052 respectively), using the single refractive index of $n_r = 1.5$ and $n_i = 0.005$.

3. Modeling Mt. Spurr ash scattering properties

To study the sensitivity of the TOMS retrieval to particle shape we used a model of a single component ash cloud composed of randomly oriented polydisperse spheroids. Spheroids are formed by rotating an ellipse along its minor (oblate spheroid) or major (prolate spheroid) axis. The shape of a spheroid is specified by the axial ratio a/b, where b is the rotational (vertical) semi-axis, and a is the horizontal semi-axis. The axial ratio is greater than 1 for oblate spheroids, smaller than 1 for prolate spheroids and equal to 1 for spheres [MT 1998]. In light of the measured 2D aspect ratios presented above, the axial ratio ranged from 0.5 to 2.5.

We assume that the total mass of the ash cloud is fixed as well as mass density, so that a particle is only allowed to change its shape without changing its volume. Thus, the size distribution of spheroids is described by the size distribution of equivalent volume spheres, n(r).

The single scattering properties of the Mt. Spurr ash cloud (extinction cross section, single scattering albedo,ω and phase matrix, γ) were computed at TOMS ash wavelengths (0.34μm, 0.36μm and 0.38μm) using the extended precision version of the T-matrix code (Mishchenko and Travis, 1998, here-after MT). For simplicity, we neglect the very slight spectral variation of refractive index at these wavelengths (Winchester 1998). The real part of the refractive index was taken from the measurements and the imaginary part was varied between 0.001 and 0.2.

3.1 Extinction cross-section

As mentioned earlier, the typical sizes of the airborne volcanic ash particles range from submicron fraction to a large ~20μm particles. Given the TOMS wavelengths in the near UV spectral region (0.34μm-0.38μm) this translates into size parameter, $x=2\pi r/\lambda$, range of less than 1 to more than 150. Figure 3 shows the monodisperse extinction efficiency factor, Q^e (Q^e = extinction cross section divided by the geometrical cross-section of the equal volume sphere, πr^2) for spheroids with different axial ratio (a/b) as a function of equivalent sphere radius. The corresponding ratios of non-spherical to spherical cross-sections are also shown in the figure. The ratios are close to 1 for finest particles (r<0.1μm), but oscillate with r for larger size particles (r> 0.1μm). The peaks in the ratios coincide with local minimums in the extinction efficiency factor for spheres. The amplitude of the oscillations increases with increase in aspect ratio. The strongest effect occurs for particle sizes comparable to the wavelength of radiation (r~0.4-0.5μm). In this size range spheroids may enhance scattering by a factor of 2 (for a/b=2.5) or more. However, just outside of this relatively narrow size range spheroids suppress scattering. This behavior suggests that averaging over broad size distribution characteristic for naturally occurring ash particles [Ref] will minimize shape effects for sub-micron fraction.

On the other hand, for micron size (coarse) fraction, the non-spherical particles systematically enhance scattering, despite the oscillations. For this reason, the shape effects remain almost as large for polydisperse particles as for monodisperse. The numerical integration over large particle sizes (r>3μm, x>50) becomes increasingly difficult, because of numerical instabilities and/or convergence problems in the T-matrix method. The maximal convergent size parameter decreases with increase in particle aspect ratio as discussed in MT [1998]. Fortunately, for large particles an opportunity appears to explore shape effects in the geometrical optics (GO) regime.

The simplicity of GO analytical expressions offers insights, which can guide and test more complex numerical calculations.

To develop such an analytical expression let us point out that the limit of the extinction cross-section for sufficiently large arbitrary shaped particle is 2G (G is the geometrical cross section for a given orientation of a particle, for sphere G $=\pi r^2$) [Hulst, 1957]. Next, we use the Cauchy theorem [Cauchy, 1841; Vouk, 1948; Chylek, 1977] that states that orientation-averaged cross-section (shadow) of any convex object is ¼A, where A is the surface area of this object. For example, for oblate spheroids:

$$\frac{Q^{\epsilon}_{spheroid}}{Q^{\epsilon}_{sphere}} = \frac{A_{spheroid}}{A_{sphere}} = \frac{1}{2}\left(1-\varepsilon^2\right)^{-1/3} + \frac{1}{4\varepsilon}\left(1-\varepsilon^2\right)^{2/3}\ln\left(\frac{1+\varepsilon}{1-\varepsilon}\right), \qquad \varepsilon^2 = 1\text{-}b^2/a^2 \qquad (1a)$$

for prolate spheroids:

$$\frac{Q^{\epsilon}_{spheroid}}{Q^{\epsilon}_{sphere}} = \frac{A_{spheroid}}{A_{sphere}} = \frac{1}{2}\left(1-\varepsilon^2\right)^{1/3} + \frac{1}{2\varepsilon}\left(1-\varepsilon^2\right)^{-1/6}\sin^{-1}(\varepsilon), \qquad \varepsilon^2 = 1\text{-}a^2/b^2 \qquad (1b)$$

Equations 1a and 1b are plotted in Figure 4 along with some points obtained via T-matrix numerical calculations. The T-matrix calculations were not possible for the true GO regime (x>>1). The points shown in figure 4 were obtained by averaging the non-spherical/ spherical T-matrix cross section ratio for monodisperse particles over the range of particle sizes from the minimal value x>30 to some maximum value (x ~90 for a/b=1.5 and x~40 for a/b=2.5). The error bars represent possible oscillations in the ratio for monodisperse particles with x>30, rather than accuracy of individual T-matrix calculations, which was better than 0.001 [MT , 1998].

The nonspherical-spherical difference in particle cross section increases monotonically with increasing deviations from sphericity because the surface area of the particle increases at a

constant volume. Indeed, at fixed volume sphere has the least surface area and, hence, produces

least possible shadow (isoperimetric property). We should stress however, that this result was

obtained for convex particles only and real ash particles can have a more complex shape.

3.2 Single scattering albedo

Volcanic plumes may increase or decrease radiation backscattered from the pure Rayleigh

atmosphere depending on the ash absorption [Krotkov et al., 1997]. The single scattering

albedo,ω, tells which part of the radiation is being scattered by the ash particles and which part is

absorbed. It is determined in turn by the particle size and complex index of refraction, m. Figure

5 shows ω at 0.380μm for monodisperse spheres and spheroids, as a function of equivalent

volume sphere radius for m=1.5-0.005i. For particle sizes comparable to wavelength of radiation

(r~0.1-0.2μm) scattering dominates absorption (ω~0.97). The absorption increases for both large

and small particles (ω decreases). In the geometrical optics limit (x>>1), the limiting value of ω

is given by [Chylek, 1975]:

$$\omega\,(x \to \infty) = \frac{1 + \left|\dfrac{m-1}{m+1}\right|^2}{2} \geq \frac{1}{2} \qquad (2)$$

This is indeed the case in figure 5, whose curve may approach 0.5 for large particles, but stays

above this value. For small particles in Rayleigh regime (x<<1) the absorption and scattering

efficiency factors (Q_{abs} and Q_{scat}) are given by equations:

$$Q_{abs} = -4x\,\mathrm{Im}\left[\frac{m^2-1}{m^2+2}\right] \sim x, \quad Q_{scat} \sim x^4 \qquad (3)$$

$$\omega(x \to 0) = Q_{scat}/(Q_{scat} + Q_{abs}) \sim x^3 \to 0$$

Since Q_{abs} is linear with x and Q_{scat} varies with x^4, the absorption dominates scattering for small values of x () (figure 5). The non-monotonic dependence of ω on r suggests that unambiguous retrieval of particle sizes is possible only for particles larger than ~0.1μm.

We also see from figure 5 that the nonspherical-spherical differences in single scattering albedo are much less pronounced than in cross section. They disappear after averaging over broad size distribution of ash particles.

3.2 Phase Function

The phase function is much more sensitive to the particle shape than are any of the other single scattering properties such as cross section or single scattering albedo [Mishenko and Travis 1995; Mischenko et al., 1996]. **Figure 6** shows a comparison of the spherical and non-spherical (a/b=1.5) single scatter phase functions, γ, at 0.380nm for polydisperse spheroids, as a function of scattering angle over the range of typical TOMS geometries. The spheroids follow a power law size distribution, n(r), r being the radius of an equivalent volume sphere. There is enhanced scattering for angles 100° to 160°. The enhanced side-scattering and suppressed backscatering may be universal characteristics of non-spherical phase functions [Mishchenko et al., 1995]. The phase function ratio increases with increasing of particle effective radius, Re. This increase at a/b=1.5 is from 1.5 for Re=0.4 μ m to 5.5 for Re=1.6 μ m. Due to the relatively small wavelength separation between the TOMS aerosol channels (20nm) and the very slight change in refractive index, there is only about a 20% difference in the phase function at 360nm and 0.380μm (for both spherical and non-spherical particles).

4. MULTIPLE SCATTERING MODEL

To compute the backscattered radiances at the TOMS sensing wavelengths (0.34μm, 0.36μm,

and 0.38μm), a single component ash cloud of spheroids following a power law size distribution,

n(r), was used to reduce the computational burden [MT 1998]. It has been shown (Hansen and

Travis, 1974; MT) that the scattering properties of most plausible size distributions, either

spherical or non-spherical particles, depend primarily upon the effective radius, Re, and the

effective variance, Ve, of the size distribution.

$$R_e = \int r^3 n(r, R_e, V_e) dr \ / \ \int r^2 n(r, R_e, V_e) dr$$

$$V_e = \int r^4 n(r, R_e, V_e) dr \ / \ \int r^2 n(r, R_e, V_e) dr$$

Though the fall-out samples have mean radii larger than 10 μm, preliminary analysis of

TOMS data using spherical particles shows the Mt. Spurr drift cloud to have Re<2 μ m (Krotkov

et al., 1998). Since the sensitivity of the TOMS retrieval to particle shape is being tested, Re was

varied between 0.1 μ m and 1.6 μ m, and Ve ranged between 0.1 and 0.73. MT have shown

there is relatively little difference between scattering properties from randomly oriented oblate

and prolate spheroids, so prolate spheroids were used here. In light of the measured 2D aspect

ratios presented above, the axial ratio of the spheroids was equal to the average measured aspect

ratio of Mt. Spurr ash samples, a/b= 1.5.

The Gauss-Seidel polarized multiple scattering radiative transfer model (Herman & Browning, 1964) was used to simulate the backscattered radiances. An underlying Lambertian surface with an albedo 0.1 was used to simulate reflection from the surface and underlying tropospheric clouds. The code was modified to input the single scattering ash phase matrix directly from the output of the T-matrix code. The radiance lookup tables were generated. In the tables, the ash optical depth at 380 nm, τ_A, was increased from 0.0 to 10.0 in steps of 1.0. The vertical distribution of the ash was modeled as a gaussian, centered at 13 km with a 1 km standard deviation, composed of homogeneous ash particles embedded in a molecular atmosphere.

Figure 7 shows the results of one such set of calculations for one particular TOMS pixel for corresponding to the Mt. Spurr conditions. Following Krotkov et al. (1997), the 0.36μ and 0.38μm normalized reflected radiances ($I_{0.36}$ and $I_{0.38}$) are plotted on a special "ash" diagram. Here the abscissa is the $-\log(I_{0.38})$ value which decreases with increasing radiance. The ratio between 0.38μm and 0.36μm channels is plotted on the ordinate in terms of $\log(\frac{I_{0.36}}{I_{0.38}})$. This is referred to as spectral contrast. Each line in the ash diagram represents the dependence of $\log(I_{0.38})$ and $\log(\frac{I_{0.36}}{I_{0.38}})$ values on ash optical thickness, τ_A for a given effective radius. The lines intersect at the point where the $\tau_A=0$. This point represents radiances, which would be measured for a pure Rayleigh atmosphere over Lambertian surface for given observational conditions (solar zenith angle $=46^\circ$, nadir viewing direction, surface albedo 0.1). As the optical depth of the

smallest particles with Re=0.1μm increases, the $\log(I_{0.38}) - \log(\frac{I_{0.36}}{I_{0.38}})$ values move along the left

branch. This line is the same for spheres and spheroids. However, larger ash particles produce the

radiances, which lie along different branches, which deviates from the Re=0.1μm line by a

change in the polar angle. Also, branches for spherical and non-spherical particles were split into

two families of curves: dashed lines (red color) represent model results for spheroids and solid

lines (blue color) represent model results for equivalent volume spheres (all other model

parameters being the same).

Gaining a qualitative understanding of this behavior can be achieved with a simple analytical

model [Krotkov et al 1997]. Let us assume a high-altitude volcanic ash layer, zero surface

albedo, small solar zenith angle, and nadir viewing direction and apply single scattering

approximation of the radiation transfer equation to approximate normalized radiance in single

channel:

$$I_\lambda = \frac{\omega \gamma_{180}}{8\pi}(1 - e^{-2\tau_A}) + e^{-2(1-\omega)\tau_A} I_\lambda^R \qquad (4)$$

where λ is the central band wavelength, I_λ^R is the normalized radiance of the Rayleigh

atmosphere for the same observational conditions, τ_A is the ash optical thickness, and γ_{180} is the

ash backscattering phase function. The first term in (4) expresses the additional backscattered

radiation from the ash layer itself, and the second term expresses the reduced radiance from the

Rayleigh atmosphere below the plume due to absorption of solar radiation by ash particles.

Due to the relatively small wavelength separation between the TOMS aerosol channels and

the very slight change in the ash refractive index, the spectral contrast for the ash term is much

smaller than for Rayleigh term ($\log(\dfrac{I^R_{0.36}}{I^R_{0.38}})$ ~0.05). Therefore, there is always a reduction in spectral contrast whenever ash particles are added to Rayleigh atmosphere. Thus, it is the ash optical thickness, which has the greatest effect on spectral contrast data.

On the other hand, the single scattering albedo mostly affects the single channel radiance [Krotkov et al., 1997]. For example, weakly absorbing ash particles tend to enhance backscattered radiance compare to that of pure Rayleigh atmosphere (see equation 4 for ω~1). For highly absorbing ash (ω<0.8) the reduced Rayleigh backscattering from the atmosphere below the plume is not compensated by ash backscattering, therefore one observes a net reduction of the backscattered radiation. This explains the effect of the particle effective radius on the polar angle in the ash diagram (figure 7). Figure 5 shows that ω decreases with r for particles larger than ~0.1μm. Therefore, increasing the particle radius (>0.1μm) is equivalent to a change from weakly absorbing to strongly absorbing ash. However, for particles with Re < 0.1μm the ω effect is reversed. Therefore the unambiguous retrieval of particle size from the UV radiances is possible for sufficiently large particles (i.e. Re >0.1μm).

We note that for observational conditions of the Spurr cloud, there is such a value of ω, that single-channel radiance remains the same for any ash optical depth. This points out a necessary condition of having at least two spectral channels for unambiguous ash retrieval optical depth-radius retrievals.

5. EFFECTS ON OPTICAL DEPTH-RADIUS RETRIEVALS

As described by Krotkov et al. (1997), τ and Re are retrieved from a diagram such as Fig. 7 by comparing measured and modeled radiance-contrast values. The particle shape has very little effect upon the ash diagram for smallest particles (Re=0.1μm). For Re > 0.1μm there is, however, a definite difference between the results for spherical and non-spherical particles. At these larger Re values the 0.38μm radiance is greater for non-spherical particles than for spherical particles, due mainly to the increased side scatter seen in Fig. 6. In addition, the spectral contrast is decreased for non-spherical particles. As a result the τ - Re retrieval, when using a spherical ash particle model, overestimates τ and underestimates Re. If the true ash particle size was 0.4 μ m, then the retrieved τ is overestimated by 10-15% and Re is underestimated by = 20%. For an ash size of 1.6 μ m and a/b= 1.5, the errors increase to 50-60% in τ 40-50% in Re.

As to the sensitivity of these differences seen in Fig.7, increasing effective variance of the size distribution,Ve, from 0.1 to 0.73, (the value used by Wen and Rose (1994) in AVHRR retrievals of Re-τ for the Mt. Spurr cloud), changes the picture very little. If the imaginary portion of the refractive index is doubled to 0.01, the error in the retrieved τ decreases to 7% at 0.4 μ m and 20% at 0.8 μ m, although the error in Re is still the same. At the moderate to low surface reflectance values (<0.3) for which this technique is applied, the results are only very weakly dependent upon the reflectance value. These results are heavily dependent upon the scattering angle and if the scan angle is increased to 48° (scattering angle = 120) then the errors decrease for e = 1.5 and increase for e = 2.0.

6. EFFECT ON MASS RETRIEVAL

The retrieved Re and τ data for each pixel can be converted to a pixel ash mass,

$$M = 4/3 \rho \tau S R_e f(R_e)$$

where p is the particle mass density, S is the pixel area, and the dimensionless mass conversion factor $f = <r^2> / <r^2 Q_e>$ (averaging over particle size distribution, f=0.5 in the geometrical optics regime). The error in the cloud mass due to particle shape is

$$\Delta M = 1 - R_e^s \tau^s f^s(R_e^s) / R_e^{ns} \tau^{ns} f^{ns}(R_e^{ns})$$

where the superscript s denotes the spherical value and ns is the non-spherical value. The difference between f^s and f^{ns} is small and can be neglected. So, the error is the ratio of the product of Re and τ. Since the errors in the retrieved Re and τ values are of opposite sign, they cancel to some degree in the mass conversion. For the case in Fig. 7 with e = 1.5 the mass is underestimated by =10%.

7. CONCLUSIONS

Using the T-matrix method of computing the scattering properties of randomly oriented spheroids, we found that shape effect is important only for sufficiently large particles (i.e. $Re > 0.1\mu m$). Polydisperse ensembles of small spheroids ($r_{eff} < 0.1\mu m$; $x < 1.6$) exhibit essentially the same scattering behavior as that of their equivalent volume spheres. This result can be expected to be true for small particles with different shapes [Pollack and Cuzzi, 1980]. On the other hand, the extinction efficiency of large polydispese spheroids ($x > 30$) differs from that of equal volume spheres by a factor equal to the ratio of their surface areas (~20% enhancement for spheroids with axial ratio $a/b=3$). The non-spherical-spherical phase function ratio can significantly deviate from unity at side-scattering angles around $130°$ and at backscattered angles. The non-spherical–spherical differences in single scattering albedo are small.

We have tested the sensitivity of the TOMS volcanic ash retrievals to the particle shape. For the case of the August 19, 1992 Mt. Spurr ash cloud and TOMS observational geometry, modeling of the ash as spherical particles causes the TOMS retrieved Re to be underestimated for $Re > 0.4\mu m$ by as much as 50%. The Re error increases with Re and is independent of τ. Generally, τ will be overestimated by as much as 50-60%. Increasing the refractive index by a factor of two decreases the errors only slightly, and changing the effective variance has a negligible effect. In terms of the total mass of the cloud, the compensating errors in Re and τ cancel somewhat and produce only about a 10% error.

8. REFERENCES

H.C.van de Hulst, Light Scattering by Small Particles (Wiley, NY, 1957), p.107

Chylek,P., Extinction cross sections of arbitrary shaped randomly oriented nonspherical particles, 1977, J.Opt.Soc. Am., 67, 1348-1350.

Hansen, J.E. and L.D. Travis, 1974, Light scattering in planetary atmospheres, Space Sci. Rev., 16, 527-610.

Herman, B.M. and S.R. Browning, 1965, A numerical solution to the equation of radiative transfer, J. Atmos. Sci. 22, 559-566.

Krotkov, N.A., O.Torres, C. Seftor, A.J. Krueger, W. Rose, A. Kostinski, G. Bluth, D.Schneider, and S.J. Schaefer, 1998, Comparison of TOMS and AVHRR volcanic ash retrievals from the August 1992 Eruption of Mt. Spurr, accepted to Geophys. Res. Let.. 1999.

Krotkov, N.A., A.J. Krueger, and P.K. Bhartia, 1997, Ultraviolet optical model of volcanic clouds for remote sensing of ash and sulfur dioxide, J. Geophys. Res., 102, 21891-21904.

Krueger, A.J. L.S. Walter, P.K. Bhartia, C.C. Schnetzler, N.A. Krotkov, I. Sprod, and G.J.S. Bluth, 1995, Volcanic sulfur dioxide measurements from the Total Ozone Mapping Spectrometer (TOMS) instruments, J. Geophys. Res., 100, 14057-14076.

Mishchenko, M.K., and L.D. Travis, 1994a, Light scattering by polydispersions of randomly oriented spheroids with sizes comparable to wavelengths of observation, Appl. Opt., 33, 7206-7225.

Mishchenko, M.I. and Travis, L.D., *J.Quant. Spectrosc. Radiat. Transfer, 1998*, **60**, 309-324

Mishchenko, M.K., Lacis, A.A., Carlson, B.E. and Travis, L.D.,Nonsphericity of dust-like tropospheric aerosols: implications for aerosol remote sensing and climate modeling, GRL, 195, v.22,1077-1080

Mishchenko, M.K., and L.D. Travis, 1994b, T-matrix computations of light scattering by large spheroidal particles, Opt. Commun. 109, 16-21.

Mishchenko, M.I., L.D. Travis, R.A. Kahn, R.A.West, Modeling phase functions for dustlike tropospheric aerosols using a shape mixture of randomly oriented polydisperse spheroids, J.Geophys. Res., 1996

Patterson, E.M., C.E.Shelden , and B.H.Stockton, Complex index of refraction between 300 and 700nm for Saharan aerosols, J.Geophys. Res., 82, 3153, 1977

Patterson, E.M., Measurements of the imaginary part of the refractive index between 300 and 700 nm for Mount St.Helens ash, Science, 211, 836, 1981

Prata, A.J., Observations of volcanic ash clouds in the 10-12μm window using AVHRR/2 data, *Int. Journ. Rem. Sens.*10, 751-776, 1989

Rose, W.I., A.B.Kostinski and L.Kelley, real time C band radar observations of 1992 eruption clouds from Crater Peak/Spurr volcano, Alaska, *U.S.Geol.Surv. Bull.* 2139,19-26, 1995

Rose, W.I., Interaction of aircraft and explosive eruption clouds: a volcanologist's perspective, AIAA Journal, 25: 52-58, 1986

Rose, W. I., and D. J. Schneider, Satellite images offer aircraft protection from volcanic ash clouds, *EOS*, 77, 529-532, 1996

Santalo, L.A., Integral Geometry and Geometric Probability, Mark Kae, editor, Addison Wesley Publishing Company, , 1976

Torres, O., P.K.Bhartia, J.R.Herman, Z.Ahmad, and J.Gleason, Derivation of aerosol properties from satellite measurements of backscattered Ultraviolet radiation: Theoretical basis, *J. Geophys. Res.*, 103, 17099-17110, 1998

Wen, S. and W.I. Rose, 1994, Retrieval of particle sizes and masses in volcanic clouds using AVHRR bands 4 and 5, J. Geophys. Res., 99, 5421-5431.

Winchester, L.W. 1998, Determination of the complex refractive index of samples of volcanic ash, NASA contract report, #S-01394-G.

Winchester, L.W., Jr., G.G. Gimmestad, R.B.Wetzel, S.M.Lee, Measurements of the phase function of natural particles, SPIE Vol.305, Atmospheric effects on Systems performance, pp. 106-118.

Figure captions

Figure 1 The backscattered Scanning Electron Microscope (SEM) image of the smallest fraction of the Wells Bay fallout sample from the August 19, 1992 Mt.Spurr eruption.

Figure 2 Frequency distribution of the measured aspect ratio for the smallest fraction of the Wells Bay fallout sample (shown in figure 1).

Figure 3. The monodisperse extinction efficiency factor, Q_e (Q_e = extinction cross section divided by the geometrical cross-section of the equal volume sphere, πr^2) for spheroids with different axial ratio (a/b) as a function of equivalent volume sphere radius, r. The ratio of nonspherical to spherical cross-section is shown at the bottom. The maximum particle size, which can be handled by the TM code, decreases with increase in particle aspect ratio [see discussion in MT, 1998].

Figure 4 The theoretical cross section ratio (spheroids/sphere) (solid lines) in geometrical optics regime (x>>1). The diamonds represent T-matrix calculations averaged over large particle sizes.

The error bars represent possible oscillations in the ratio for monodisperse particles with x>30, rather than accuracy of the individual T-matrix calculations, which was better than 0.001 [MT , 1998].

Figure 5 Single scattering albedo for monodisperse randomly oriented spheroids with different axial ratios vs radius.

Figure 6 The ratio of non-spherical (a/b=1.5) to spherical phase functions at 380nm as a function of the scattering angle for different particle sizes (given by effective radius, Re of the equivalent spheres size distribution). The index of refraction is from the Mt.Spurr ash sample and effective variance of the size distribution is 0.1.

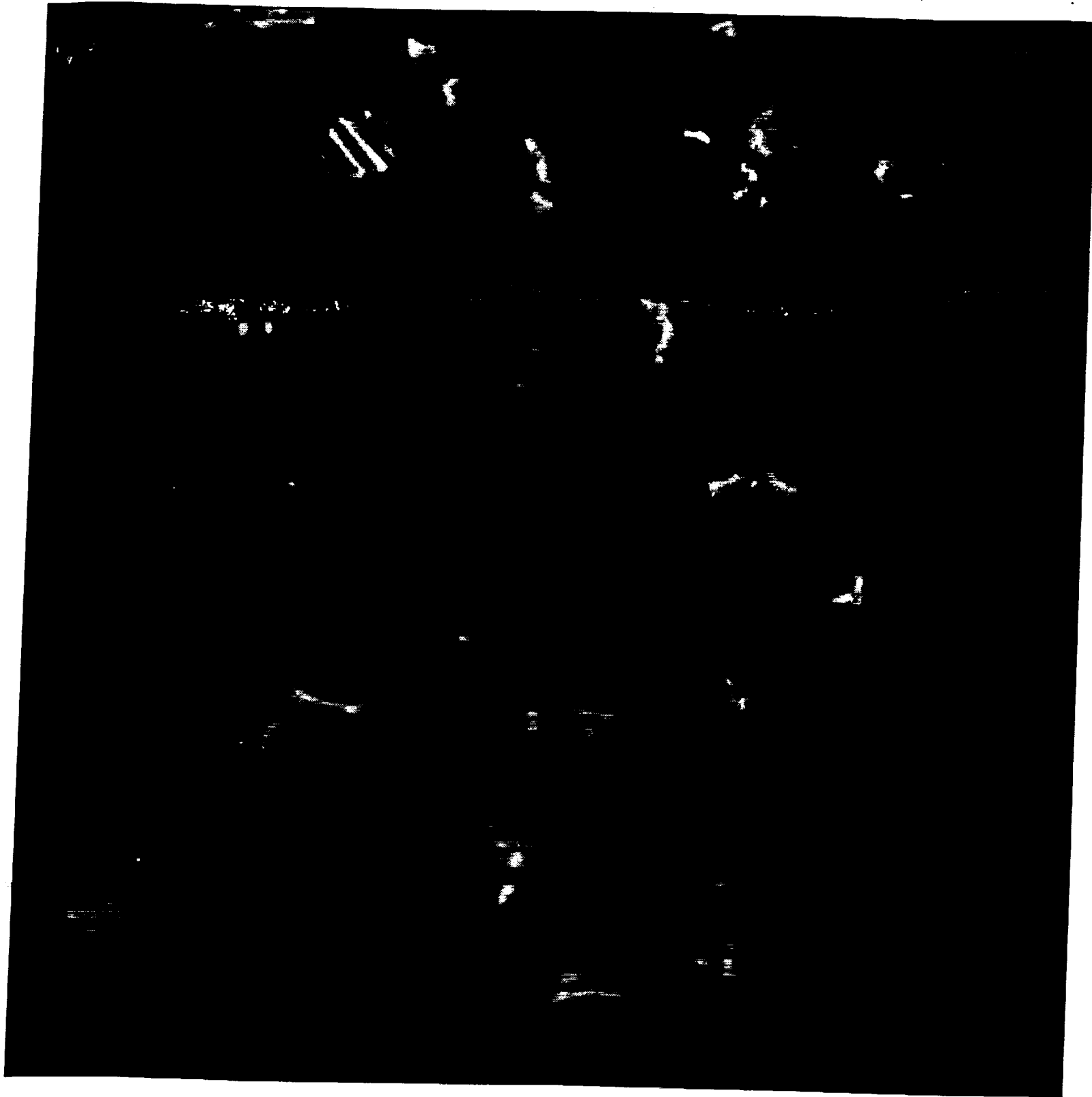Figure 7 The TOMS ash diagram for spheroidal particle shapes with different axial ratios. Dashed lines (red) correspond to a/b=1.5 and the solid lines (blue) correspond to spheres (a/b=1). The observational conditions are solar zenith angle =46o , nadir viewing and surface reflectance of 0.1.

The black asterisk shows actual TOMS measurements for this particular pixel.

Table 1 The measured aspect ratios (AS) for different particle sizes in the Wells Bay sample. The air flow rate was adjusted to obtain 18 groups of particles with different terminal settling velocities (i.e. tvg 1 corresponds to terminal velocity group 1 etc.), so that the lowest numbered terminal velocity group corresponds to the smallest spherical equivalent (se) particle radius. For all particles: number of cases=1297; min. AS=1.398, max.AS=1.642, mean AS=1.498; standard deviation =0.066.

	tvg1	tvg2	tvg3	tvg4	tvg5	tvg6
se	0-10	10-15	15-20	20-25	25-30	30-35
cases	112	43	79	47	51	61
min	1.100	1.180	1.110	1.140	1.120	1.060
max	2.460	2.670	2.370	2.810	3.560	2.480
mean	1.558	1.515	1.530	1.551	1.572	1.476
dev.	0.321	0.316	0.283	0.315	0.401	0.295

(cont)	tvg7	tvg8	tvg9	tvg10	tvg11	tvg12
se	35-40	40-45	45-50	50-55	55-60	60-65
cases	89	47	45	55	91	145
min	1.080	1.160	1.120	1.100	1.090	1.060
max	2.670	4.570	3.560	1.860	2.210	2.360
mean	1.483	1.642	1.579	1.405	1.471	1.470
dev.	0.271	0.616	0.431	0.194	0.277	0.250

(cont)	tvg13	tvg14	tvg15	tvg16	tvg17	tvg18
se	65-70	70-75	75-80	80-85	85-90	>90
cases	129	51	49	76	68	59
min	1.090	1.140	1.130	1.140	1.060	1.100
max	3.130	2.600	2.210	2.930	2.230	2.280
mean	1.451	1.529	1.464	1.462	1.398	1.412
dev.	0.292	0.300	0.282	0.275	0.249	0.231

Fig 1

Fig 2

Number of measurements

Aspect Ratio